Available online at www.sciencedirect.com
SCIENCE DIRECT®
International Journal of Thermal Sciences 44 (2005) 121–135
International Journal of Thermal Sciences
www.elsevier.com/locate/ijts

Mixed convection in a shallow enclosure with a series of heat generating components

Mayur T. Bhoite, G.S.V.L. Narasimham *, M.V. Krishna Murthy [1]

Department of Mechanical Engineering, Indian Institute of Science, Bangalore 560 012, India

Received 4 November 2003; received in revised form 8 June 2004; accepted 8 June 2004

Abstract

The problem of mixed convection flow and heat transfer in a shallow enclosure with a series of block-like heat generating components is studied numerically for a range of Reynolds and Grashof numbers and block-to-fluid thermal conductivity ratios. The flow and temperature distributions are taken to be two-dimensional. Regions with the same velocity and temperature distributions can be identified assuming repeated placement of the blocks and fluid entry and exit openings at regular distances, neglecting end wall effects. One half of such a rectangular region is chosen as the computational domain taking into account the symmetry about the vertical centerline. On the basis of the assumption that mixed convection inlet velocity can be treated as the superposition of forced convection and natural convection velocities at the inlet and that mixed convection pressure drop across the enclosure is due to the forced flow contribution alone, the individual flow components are delineated. The Reynolds number is based on forced convection velocity, which can be determined in practice from the fan characteristics. This is believed to be more meaningful unlike the frequently used total velocity based Reynolds number, which does not vanish even in pure natural convection and which makes the fan selection difficult. The results show that higher Reynolds numbers tend to create a recirculation region of increasing strength at the core region and that the effect of buoyancy becomes insignificant beyond a Reynolds number of typically 600. Results are also presented for a number of quantities of interest such as the flow and temperature distributions, local and average Nusselt numbers and the maximum dimensionless temperature in the block.

Keywords: Mixed convection; Enclosure; Volumetric heat generation; Pressure drop

1. Introduction

Combined free-forced or mixed convection is the name given to that régime of convective heat transport in which there is a significant interaction between forced and free convection effects. Mixed convection can occur both in external flows and in internal flows. The parameter of importance in mixed convection is the Archimedes number $Ar(= Gr/Re^2)$. The heat transfer mechanism is predominantly forced convection or free convection according as $Ar \ll 1$ or $Ar \gg 1$. When $Ar \approx 1$, both the mechanisms become important. The external flow mixed convection problems have been first studied by van der Hegge Zijnen [1] and Acrivos [2]. Mixed convection heat transfer over submerged bodies and in channels/ducts has received considerable attention in the literature as revealed in the reviews by Chen et al. [3], Churchill [4] and Aung [5]. Chen et al. [3] present correlating equations for Nusselt number in mixed convection over plates, cylinders and continuously moving sheets. Relations for $Nu/Re^{1/2}$ in mixed convection over isothermal vertical flat plates and cylinders are presented in terms of Ar, and for horizontal plates and continuously moving sheets in terms of $Gr/Re^{5/2}$. By means of a scale analysis, Bejan [6] shows that $Nu/(Re^{1/2}Pr^{1/3})$ in mixed convection over an isothermal vertical flat plate correlates well with the

* Corresponding author.
E-mail addresses: mayur@mecheng.iisc.ernet.in (M.T. Bhoite), mecgsvln@mecheng.iisc.ernet.in (G.S.V.L. Narasimham), mvk@mecheng.iisc.ernet.in (M.V.K. Murthy).
[1] Present address: Director, Energy Research Centre, Vellore Institute of Technology, Vellore 632014, India.

1290-0729/$ – see front matter
doi:10.1016/j.ijthermalsci.2004.07.003

Nomenclature

a	thermal diffusivity of the fluid	$m^2 \cdot s^{-1}$
Ar	Archimedes number, $= Gr\,Re^{-2}$	
c_p	constant pressure specific heat capacity of the fluid	$J \cdot kg^{-1} \cdot K^{-1}$
c_s	specific heat capacity of the solid	$J \cdot kg^{-1} \cdot K^{-1}$
g	gravitational acceleration	$m \cdot s^{-2}$
Gr	Grashof number, $= g\beta\Delta T H^3/\nu^2$	
H	Height of the enclosure	m
H_1	Height of the heat generating block	m
L_i $(i = 1, \ldots, 4)$	various horizontal dimensions in Fig. 1(c)	m
n	distance measured normal to block surface into the fluid	m
Nu_{local}	local Nusselt number (Eq. (11))	
Nu_1	average Nusselt number (Eq. (12))	
Nu_2	Nusselt number based on maximum temperature (Eq. (14))	
p	excess pressure over the hydrostatic	Pa
Pe	Péclet number, $= Re\,Pr$	
Pr	Prandtl number, $= \nu/a$	
$\dot{Q}_v$	volumetric heat generation rate in the solid	$W \cdot m^{-3}$
Ra	Rayleigh number, $= Gr\,Pr$	
Re	Reynolds number, $= v_{\text{in,fc}} H/\nu$	
s	distance measured along the periphery CDE of the block starting from C (Fig. 1(c))	m
t	time	s
T	temperature	K
u, v	velocity components in the x-direction and y-direction	$m \cdot s^{-1}$
x, y	Cartesian coordinates	m

Greek symbols

α	heat transfer coefficient	$W \cdot m^{-2} \cdot K^{-1}$
β	volumetric expansion coefficient of the fluid	K^{-1}
γ	angle made by channel wall with the gravity vector [21]	degrees
Δp	pressure drop across the enclosure	Pa
ΔT	characteristic temperature difference, $= \dot{Q}_v H^2/\lambda$	K
λ	thermal conductivity of the fluid	$W \cdot m^{-1} \cdot K^{-1}$
λ_s	thermal conductivity of the solid	$W \cdot m^{-1} \cdot K^{-1}$
ν	kinematic viscosity of the fluid	$m^2 \cdot s^{-1}$
ρ	density of the fluid	$kg \cdot m^{-3}$
ρ_s	density of the solid	$kg \cdot m^{-3}$
ψ	stream function, $= \psi_{\text{ref}} + \int (u\,dy - v\,dx)$	$m^2 \cdot s^{-1}$

Subscripts

bs	block surface
fc	forced convection
local	local quantity on the block surface
in	inlet
max	maximum
nc	natural convection contribution in mixed convection
out	outlet
pnc	pure natural convection
ref	reference
s	solid

Superscript

$*$	dimensionless quantity

parameter $Ra^{1/4}/(Re^{1/2}Pr^{1/3})$ when $Pr > 1$ and with the parameter $Bo^{1/4}/Pe^{1/2}(= Ar^{1/4})$ when $Pr < 1$, where the Boussinésq number Bo is the product of the Rayleigh number and the Prandtl number $Ra\,Pr$ or $Gr\,Pr^2$. Metais and Eckert [7] have presented régime maps for horizontal and vertical ducts, with abscissa $Gr\,Pr(D/L)$ or $Gr\,Pr$, and ordinate Re, for delineating the laminar and turbulent, forced, free and mixed convection regions. This remains the most important work for the prediction of flow régimes in mixed convection duct flow. Dalbert [8] has prepared régime diagrams for aiding laminar mixed convective flow in channels.

In thermal energy storage tanks, the water extracted from the tank undergoes heating in solar collectors or other equipment and the heated water is returned to the tank. In these instances, the interaction between forced and free convection becomes important as shown, for instance, by Chan et al. [9]. Mixed convection occurring in water bodies like lakes and ponds due to thermal discharges is studied by Oberkampf and Crow [10], who have systematically taken into account the effects of inflow/outflow, wind shear, buoyancy and heat losses from the surface by convection, evaporation and radiation. In air-conditioned rooms, the buoyancy created due to human occupancy influences the forced air circulation to a significant extent as reported by Nielsen et al. [11].

Combined free-forced convection in electronics cooling has also received considerable attention in the literature. Oosthuizen and Paul [12] have investigated mixed convection heat transfer in a cavity with uniformly heated, isothermal vertical walls and horizontal adiabatic walls. A forced flow, with either aiding or opposing effect on the buoyancy, enters and leaves the enclosure across the cold wall. The heat transfer results obtained at various values of Grashof number and the aspect ratio of the cavity are compared with the pure natural convection case. In the study of Simoneau et al. [13], the forced flow enters a shallow enclosure through the hot wall and leaves through the opposite cold wall. Again, both aiding and opposing flow circumstances are investigated and the results are compared with the asymptotic cases of forced

convection and pure natural convection. Mixed convection transport from an isoflux heat source attached to an enclosure wall has been studied numerically by Papanicolaou and Jaluria [14]. The authors have studied the effects of the positioning of the heat source and outlet opening on the flow pattern and temperature distribution. Results are presented for the maximum temperature attained by the heat source. The study has also been extended to encompass the effects of wall heat conduction, protruding heat sources and transition from steady laminar régime to a periodic régime [15–17]. Further study devoted to the transition process has revealed that mixed convection may become unstable beyond a critical value of the Archimedes number. The instability due to localised heating is found to affect the temperature distribution all over the enclosure, while affecting the flow field mainly in the core region of the enclosure. The frequency of the thermal oscillations is found to be an increasing function of the Grashof number and a decreasing function of the Reynolds number. In particular, the Reynolds number is found to have a stabilising effect, suggesting that the instability is of a thermal origin. Computations of turbulent flow inside the enclosure [18] have revealed that most of the turbulence develops near the right vertical wall of the cavity, opposite to the location of the heat source and near the outflow opening. The production of turbulence at that location is predominantly due to shear. A small amount of turbulence is generated due to buoyancy, along the left vertical wall, right above and in the thermal boundary of the heat source. The average Nusselt number from the source is only slightly affected by the Reynolds number and is found to vary as $Gr^{0.26}$, in the range of $1 \times 10^7 \leqslant Gr \leqslant 5 \times 10^8$, which is close to the numerically and experimentally derived correlations for pure natural convection in closed cavities. Transient laminar mixed convection in a partitioned enclosure with an isoflux heat source embedded on a vertical wall has been investigated numerically by How and Hsu [19]. They have found that the time required for the attainment of steady state and the transient behavior depend strongly on the governing parameters and the configuration of the divider. Hsu and Wang [20] have investigated numerically mixed convection in a enclosure with discrete isoflux heat sources placed on a baffle of finite thickness. If the heat sources face the outlet, the Nusselt number is found to be independent of the location of the sources, while sources placed to face the inlet have been found to result in considerable variation in the Nusselt number. Higher thermal conductivity of the baffle enhances the cooling of the sources. The papers by Choi and Ortega [21] and Kennedy and Zebib [22] represent typical studies of mixed convection in channels with discrete heat sources. Mixed convection in other geometries and applications has also received some attention [23,24].

The objective of present analysis is to investigate the mixed convection heat transfer in a shallow enclosure with a series of floor-mounted block-like heat generating components and with multiple floor admission and ceiling extraction openings. The enclosure can be visualised to represent an electronic cabinet with electronic packages or an air-conditioned computer room. The components and openings are deployed in such a way that, neglecting end wall effects, they form a series of domains in which flow and temperature fields are identical. In addition, in each such domain, there is a symmetry about the vertical centreline, enabling one half of the domain to be considered for analysis. In the earlier studies on mixed convection, the inlet velocity to the enclosure, containing contributions from both forced and natural convection, is taken as the characteristic velocity. However, in this paper, a more convenient approach of basing the Reynolds number on the forced convection component alone, is adopted.

2. Physical model and computational domain

Fig. 1(a) shows the physical model of the shallow enclosure consisting of a series of heat generating components (although for simplicity only three are shown), floor admission openings for conditioned air and ceiling extraction openings for exhaust air. The analysis assumes the heat source to be a solid block with uniform and time-invariant heat generation. At times less than or equal to zero, the fluid inside the enclosure is assumed to be quiescent with uniform temperature. For times greater than zero, the admission of conditioned air, extraction of used air and volumetric heat generation within the block are initiated. A rectangular velocity profile is assumed for the inlet air. The inlet velocity is the sum of forced and natural convection components. The enclosure can be divided into a number of modules in which the flow and temperature distributions are identical, assuming that the effects of leftmost and rightmost end modules are negligible (Fig. 1(b)). Moreover, for simplicity, the flow and temperature fields are taken to be two-dimensional, assuming negligible variation in a direction perpendicular to the plane of the figure. For this assumption to be reasonable, the inlet and outlet openings should resemble transverse slots and the heat generating devices should resemble transverse rib-like components. The objectives of the work are to find the temperature and velocity distributions inside the enclosure and the maximum temperature inside the block, which helps to ascertain whether the device represented by the block is working within the safe temperature limit. Since there is a symmetry of flow and temperature distributions about the vertical centreline in each module (for instance, about the line LP in the module marked with letter symbols), one half of a module can be taken as the computational domain as shown in Fig. 1(c), in which the origin is placed at the bottom left corner with positive direction of the x-axis towards right and positive direction of the y-axis vertically upwards. The gravity vector is oriented parallel to the y-axis with an opposite sense.

The choice of limiting the computational domain to a rectangular region introduces the free boundaries AB and ML at the inlet and outlet as shown in Fig. 1(c). Specification

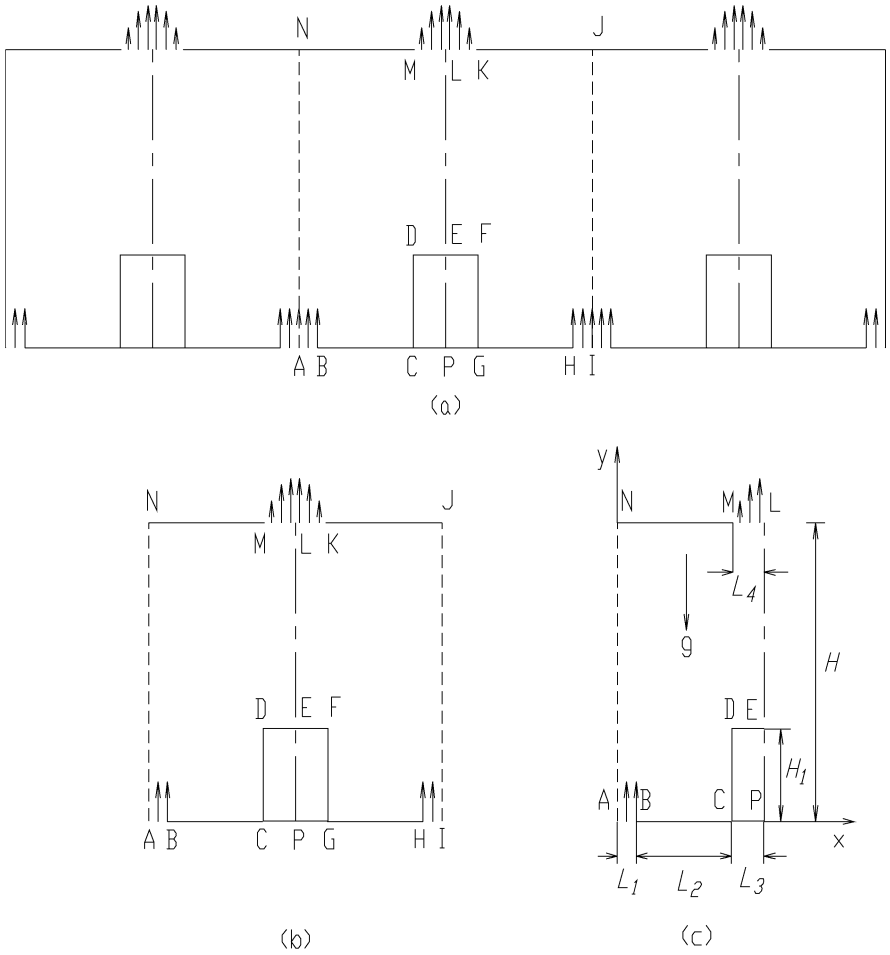

Fig. 1. (a) Physical model, (b) A module containing heat source, (c) Computational domain.

of accurate boundary conditions on these free boundaries is difficult because of the effect of duct extensions or plenums that may exist beyond the inlet and outlet. On the other hand, the computational effort becomes more involved if the domain is extended to include the upstream and downstream geometrical details. Hence in the interest of eliminating the specific geometrical details beyond the inlet and outlet and yet obtain flow and temperature predictions of reasonable accuracy, a simpler domain is chosen with specification of plausible boundary conditions on the free boundaries.

3. Mathematical formulation

3.1. Governing equations

The flow and temperature distributions are governed by continuity, Navier–Stokes and, fluid and solid energy equations. The radiative heat transfer, viscous heat dissipation and compressibility effects of air are considered to be negligible. The effect of the density variation causing the buoyancy force is taken into account through the Oberbeck–Boussinésq approximation. Other thermophysical properties of the fluid and the thermophysical properties of the solid are assumed to be independent of temperature.

The governing equations in non-dimensional form read:

$$\frac{\partial u^*}{\partial x^*} + \frac{\partial v^*}{\partial y^*} = 0 \tag{1}$$

$$\frac{\partial u^*}{\partial t^*} + u^*\frac{\partial u^*}{\partial x^*} + v^*\frac{\partial u^*}{\partial y^*} = -\frac{\partial p^*}{\partial x^*} + \left(\frac{\partial^2 u^*}{\partial x^{*2}} + \frac{\partial^2 u^*}{\partial y^{*2}}\right) \tag{2}$$

$$\frac{\partial v^*}{\partial t^*} + u^*\frac{\partial v^*}{\partial x^*} + v^*\frac{\partial v^*}{\partial y^*} = -\frac{\partial p^*}{\partial y^*} + \left(\frac{\partial^2 v^*}{\partial x^{*2}} + \frac{\partial^2 v^*}{\partial y^{*2}}\right) + Gr\,T^* \tag{3}$$

$$\frac{\partial T^*}{\partial t^*} + u^*\frac{\partial T^*}{\partial x^*} + v^*\frac{\partial T^*}{\partial y^*} = \frac{1}{Pr}\left(\frac{\partial^2 T^*}{\partial x^{*2}} + \frac{\partial^2 T^*}{\partial y^{*2}}\right) \tag{4}$$

$$\rho_s^* c_s^* \frac{\partial T_s^*}{\partial t^*} = \frac{\lambda_s^*}{Pr}\left(\frac{\partial^2 T^*}{\partial x^{*2}} + \frac{\partial^2 T^*}{\partial y^{*2}}\right) + \frac{1}{Pr} \tag{5}$$

The definitions of the various quantities appearing in the above equations are as follows:

$$x^* = \frac{x}{H}, \qquad y^* = \frac{y}{H}, \qquad t^* = \frac{t\nu}{H^2}$$

$$u^* = \frac{uH}{\nu}, \qquad v^* = \frac{vH}{\nu}, \qquad p^* = \frac{pH^2}{\rho\nu^2}$$
$$T^* = \frac{T - T_{\text{in}}}{\Delta T}, \quad \text{where } \Delta T = \frac{\dot{Q}_v H^2}{\lambda}, \; Pr = \frac{\nu}{a}$$
$$\rho_s^* = \frac{\rho_s}{\rho}, \qquad c_s^* = \frac{c_s}{c_p}, \qquad \lambda_s^* = \frac{\lambda_s}{\lambda} \tag{6}$$

The geometrical parameters are defined as follows:

$$L_1^* = \frac{L_1}{H}, \qquad L_2^* = \frac{L_2}{H}, \qquad L_3^* = \frac{L_3}{H}$$
$$L_4^* = \frac{L_4}{H}, \qquad H_1^* = \frac{H_1}{H}, \qquad L^* = L_1^* + L_2^* + L_3^* \tag{7}$$

3.2. Initial and boundary conditions

The initial conditions (corresponding to $t^* \leqslant 0$) are $u^* = v^* = T^* = T_s^* = 0$ throughout the computational domain. The hydrodynamic and thermal boundary conditions (corresponding to $t^* > 0$) can be stated as follows:

The hydrodynamic boundary conditions for the mixed/forced convection problem for the fluid region ABCDELMNA are zero normal gradients of normal and tangential velocities on the symmetry boundaries AN and EL, no slip and mass impermeability on the solid boundaries BC, CD, DE and MN, prescribed dimensionless velocity at the inlet AB with time-invariant and rectangular profile and prescribed pressure at the exit LM. The thermal boundary conditions for the fluid region ABCDELMNA are zero dimensionless temperature at the inlet AB, zero normal gradient of temperature on the symmetry boundaries AN and EL, zero normal gradient of temperature at the exit LM, no temperature jump and heat flux continuity on the solid–fluid interfaces CD and DE and adiabatic condition on BC and MN. For the solid domain CPEDC, adiabatic conditions are used on the boundaries CP and PE and heat flux continuity with no temperature jump is prescribed on CD and DE.

In mixed convection, the dimensionless inlet velocity v_{in}^* can be written as:

$$v_{\text{in}}^* = Re + v_{\text{in,nc}}^* \tag{8}$$

where the Reynolds number Re is defined as $v_{\text{in,fc}}H/\nu$ ($v_{\text{in,fc}}$ being is the forced convection inlet velocity) and the dimensionless natural convection inlet velocity $v_{\text{in,nc}}^*$ is defined as $v_{\text{in,nc}}H/\nu$ ($v_{\text{in,nc}}$ being the natural convection inlet velocity in the mixed convection case).

The forced convection velocity $v_{\text{in,fc}}$ corresponds to the velocity produced by the fan in isothermal flow and the natural convection velocity $v_{\text{in,nc}}$ corresponds to that induced by the buoyancy effect. The basic assumption in this paper is that the mixed convection inlet velocity can be treated as a super-imposition of forced convection inlet velocity over natural convection inlet velocity. Accordingly, any mixed convection pressure drop Δp^* produced across the enclosure is due to the forced flow contribution alone and the forced and mixed convection pressure drops for the same Re would not be different. The pressure drop here is defined as:

$$\Delta p^* = \frac{1}{L_1^*}\int_{\text{inlet}} p^*\,\mathrm{d}x^* - \frac{1}{L_4^*}\int_{\text{outlet}} p^*\,\mathrm{d}x^* \tag{9}$$

The natural convection is entirely driven by buoyancy and it does not produce any pressure drop across the enclosure. This is applicable when the flow is inducted from and exits into atmosphere or plenums which are substantially at constant pressure. Although pressure defects of small magnitude may occur at the inlet and outlet, the zero global pressure drop assumption appears to yield realistic natural convection predictions in case of vertical ducts/channels [25,26] and open/vented enclosures [27,28]. Following these studies equal inlet and outlet pressures are assumed in the present study while solving for pure natural convection. However, in cases where the natural convection flow enters the enclosure from an elaborate suction manifold, an estimate of the depression of the inlet pressure over that of the exit is desirable to obtain accurate results.

To proceed with the solution, first the pure forced convection problem with $v_{\text{in}}^* = Re$ and $Gr = 0$ can be solved for various values of Re and a correlation can be established between the pressure drop Δp^* and Re. The mixed convection problem is then solved for a prescribed dimensionless total inlet velocity v_{in}^* and Gr, and the pressure drop Δp^* is determined. Since by assumption, the mixed and forced convection pressure drops are the same for a given Reynolds number, the value of Re in mixed convection can be found using the forced convection correlation relating the pressure drop and the Reynolds number. The quantity $v_{\text{in,nc}}^*$ (denoting the dimensionless average natural convection inlet velocity in the mixed convection case) can be determined by subtraction, i.e., $v_{\text{in,nc}}^* = v_{\text{in}}^* - Re$. For $Re = 0$ and a given Gr, the dimensionless pure natural convection inlet velocity $v_{\text{in,pnc}}^*$ can be separately determined by solving the natural convection problem with equal pressure values at the inlet and the outlet and taking the average of the vertical velocity across the inlet. It should be noted that for the same value of Gr, the mixed and pure natural convection quantities $v_{\text{in,nc}}^*$ and $v_{\text{in,pnc}}^*$ cannot be expected to be the same because of the differing temperature distributions in mixed convection and pure natural convection for the same Gr.

In the literature on mixed convection problems one frequently comes across the definition of Reynolds number based on the total velocity v_{in} which is the sum of the velocities $v_{\text{in,fc}}$ and $v_{\text{in,nc}}$. Since the flow rate versus the pressure drop characteristic of a fan can yield only $v_{\text{in,fc}}$ but not v_{in}, with such a definition of Reynolds number, the selection of an appropriate fan in a practical situation becomes very difficult. Secondly, the quantity Re, which is conventionally a forced convection parameter, would be non-zero even in the pure natural convection case because v_{in} remains finite. The decomposition of the inlet velocity into forced and natural convection components, as is done in the present paper, is

believed, apart from exhibiting more clearly the characteristics of the mixed convection, to be more helpful in practical applications.

3.3. Nusselt numbers

The local heat transfer coefficient at any location on the block surface can be defined with the aid of the relation:

$$\alpha_{\text{local}}(T_{\text{bs}} - T_{\text{in}}) = -\lambda\left(\frac{\partial T}{\partial n}\right)_{\text{bs}} \tag{10}$$

where n denotes the distance measured normal to the block surface into the fluid and the subscript bs denotes the block surface. The local Nusselt number is given by:

$$Nu_{\text{local}} = \frac{1}{T^*_{\text{bs}}}\left(\frac{\partial T^*}{\partial n^*}\right)_{\text{bs}} = \frac{\dot{q}_{\text{bs}}}{T_{\text{bs}} - T_{\text{in}}} = \frac{\dot{q}^*_{\text{bs}}}{T^*_{\text{bs}}} \tag{11}$$

The average Nusselt number $Nu_1 (= \alpha_1 H/\lambda)$ may be defined in the conventional fashion as:

$$Nu_1 = \frac{1}{s^*_{\text{bs}}} \int_0^{H_1^* + L_3^*} Nu_{\text{local}}\, \mathrm{d}s^* \tag{12}$$

where s^* is the dimensionless distance measured along the periphery of the block.

However, since this is a problem involving known heat generation rate in the block, it is more useful to define an average heat transfer coefficient α_2 based on the maximum temperature of the block as follows:

$$\alpha_2(H_1 + L_3)(T_{\max} - T_{\text{in}}) = \dot{Q}_v H_1 L_3 \tag{13}$$

which gives:

$$Nu_2 \equiv \frac{\alpha_2 H}{\lambda} = \frac{H_1^* L_3^*}{H_1^* + L_3^*}\frac{1}{T^*_{\max}} \tag{14}$$

Thus Nu_2 is a measure of the reciprocal of the maximum dimensionless temperature in the block.

4. Method of solution

A numerical formulation is developed by discretising the primitive variable equations on a staggered mesh. The grid is such that the pressure and temperature nodes are placed midway between the velocity nodes. Boundary conditions are set via an extra layer of pseudo-cells. For the estimation of the allowable time step, guidance is obtained from the Courant–Friedrichs–Lewy and diffusive restrictions [28].

It is desirable to employ a high accuracy scheme for the convective terms of the momentum equations [29]. Hence these are discretised using a hybrid linear-parabolic approximation developed by Zhu [30]. This scheme has the desirable features like third order accuracy, boundedness and low false diffusion. The diffusive terms of the momentum equations and the solid energy equation are discretised with central differences. The combined convective and diffusive flux in the fluid energy equation is approximated by a power-law scheme [31].

The pressure-velocity coupling is handled using an implicit version of the SMAC (Simplified Marker and Cell) method [32] combined with an iterative time advancement strategy, in which sufficient number of global iterations are performed over the same time step on the discretised equations. Line-by-line sweeps are performed with the tridiagonal matrix algorithm, by obtaining the solution for all the grid points on a horizontal line at a time. When solving for the temperature, if a line of grid points involves both solid and fluid regions, the temperature in the two regions is obtained simultaneously, by an appropriate modification of the discretised energy equations for control volumes on either side of the interface. The heat flux continuity at the solid–fluid interfaces is effected via the harmonic mean thermal conductivity method of Patankar [31].

For the natural convection problem, the boundary conditions are applied in such way that pressure drop through the enclosure becomes equal to zero while velocities at inlet and outlet are calculated using the continuity constraint. Since the steady state results are of interest in the present paper, the thermal capacitance of the solid during some runs is chosen such that faster convergence to steady state is obtained. Convergence to steady state is monitored by relative error criteria. Based on preliminary numerical experimentation, a relative error criterion of 10^{-5} on dimensionless velocities and an absolute criterion of 10^{-6} on dimensionless temperature are found to be satisfactory. The overall energy balance on the computational domain is used as an additional check for the attainment of steady state.

By incorporating the above mentioned features, a computer program is written in Fortran 90 to solve the present problem. Results are obtained by running the code on an ALPHA server. The computer program is validated by reproducing the results of published papers on mixed convection in enclosures [14] and channels [21,22] with wall-mounted thin isoflux heaters and natural convection in an air-filled differentially heated square cavity [33]. As shown in Table 1, the published results compare favourably with the results reproduced using the present computer program. Kennedy and Zebib [22] studied mixed convection in a horizontal channel with discrete heating of the bottom plate and/or upper plate for various sizes and placements of the heat sources. They obtained numerical results using parabolic equation model for one case with the dimensionless channel length 49.8 and with discrete heating of the bottom plate extending over a dimensionless length of 11.5 starting from the entry of the channel. For the other cases, they used an elliptic equation model (i.e., the model with full equations in two-dimensions) for the numerical solution. Detailed experimental temperature distributions over the heat source length were presented for the case solved with parabolic equation model, for various values of κ $(= 4\,Gr/Re^2$, where Gr is the Grashof number based on heat flux and channel width and Re is the Reynolds number based on channel width),

Table 1
Validation results of the present program against published papers

Parameters	Papanicolaou and Jaluria (P & J) [14]			
	T^*_{max}		Nu	
	P & J	Present	P & J	Present
$Re = 50$, $Ar = 0.04$	0.99	0.946	1.10	1.096
$Re = 50$, $Ar = 0.4$	0.69	0.663	1.4	1.288
Parameters	Choi and Ortega (C & O) [21], $Gr = 10^4$			
	T^*_{max}		Nu	
	C & O	Present	C & O	Present
$Re = 1$, $\gamma = -90°$	0.5	0.520	5.5	5.024
$Re = 5$, $\gamma = -90°$	0.42	0.431	2.7	2.692
$Re = 50$, $\gamma = -90°$	0.22	0.248	5.75	5.690
$Re = 50$, $\gamma = +90°$	0.22	0.250	5.5	5.290
Ra	de Vahl Davis (dVD) [33]			
	Nu		ψ^*_{max}	
	dVD	Present	dVD	Present
10^5	4.509	4.562	9.612	9.636
10^6	8.817	8.953	16.75	16.740

Table 2
Sensitivity of the results to different grids

Grid size[+]	Pure natural convection ($\lambda^*_s = 100$)			
	$Gr = 10^5$		$Gr = 5 \times 10^6$	
	$v^*_{in,pnc}$	T^*_{max}	$v^*_{in,pnc}$	T^*_{max}
50×50	31.53	0.0379	203.80	0.0363
50×75	36.91	0.0342	218.72	0.0364
60×75	36.50	0.0341	213.63	0.0367
75×75	36.15	0.0341	207.76	0.0368
Grid size[+]	Mixed convection (MC) and forced convection (FC)			
	$\lambda^*_s = 100$, $v^*_{in} = 1710$ $Gr = 5 \times 10^6$ (MC)		$\lambda^*_s = 100$, $v^*_{in} = Re = 1500$ $Gr = 0$ (FC)	
	$\Delta p^*/Re^2$	T^*_{max}	$\Delta p^*/Re^2$	T^*_{max}
50×50	0.5803	0.0082	0.4639	0.0089
50×75	0.6787	0.0085	0.5270	0.0092
60×75	0.6805	0.0085	0.5282	0.0092
75×75	0.6838	0.0084	0.5306	0.0091

[+] Number of control volumes in x^* and y^* directions, respectively.

although a limited amount of experimental data was also presented for two other cases. Hence, the case of isoflux bottom plate heating over the dimensionless length of 11.5 units from the entry is chosen for validating the present code and the results are shown in Fig. 2. While there is a good agreement between the computed and measured distributions for $\kappa = 0.06$ and 0.156, the measured results for $\kappa = 0.28$ reveal a more uniform distribution due probably to pronounced channel plate conduction. Moreover, the temperatures computed from the present code are considerably less than those computed by Kennedy and Zebib [22] using a parabolic equation model for $\kappa = 0.28$. Although measured temperature distribution was also presented for $\kappa = 0.57$, our code did not produce steady converged results for this case. This could be due to the formation of vortex rolls downstream of

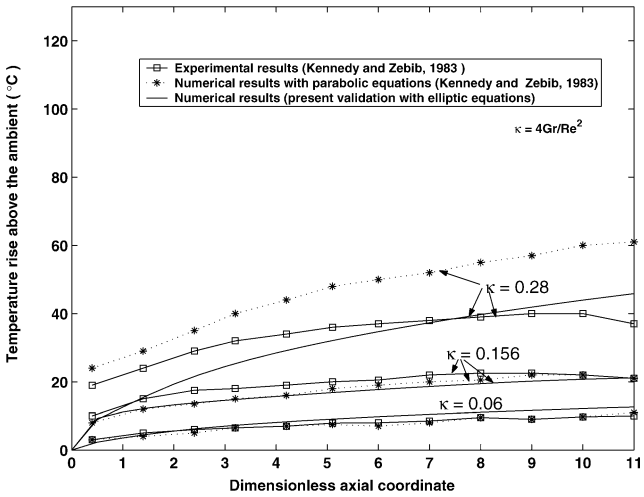

Fig. 2. Validation of present code against the experimental and numerical results by Kennedy and Zebib [22].

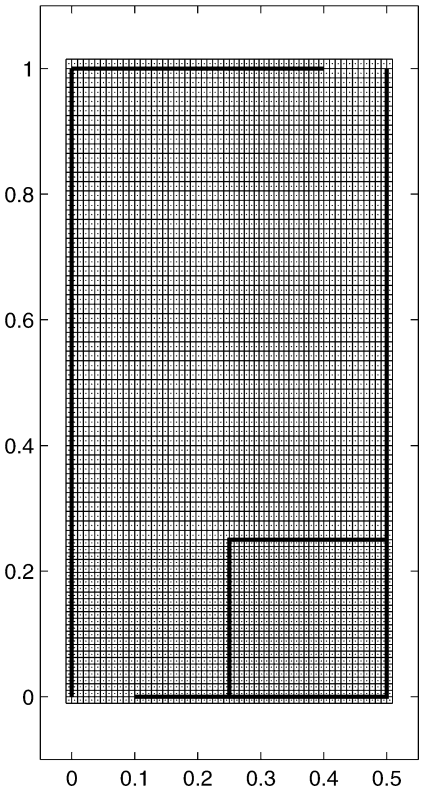

Fig. 3. Grid point distribution in the 60×75 mesh.

the heat source as observed experimentally by Kennedy and Zebib [22].

In order to select the grid sizes which yield reasonably accurate predictions, grid sensitivity tests are conducted with $Pr = 0.7$, $L^*_1 = 0.1$, $L^*_2 = 0.15$, $L^*_3 = 0.25$, $L^*_4 = 0.1$ and $H^*_1 = 0.25$. Based on the results shown in Table 2, a 60×75 is grid is adopted as a compromise between accuracy and computing time. The distribution of the grid points is shown in Fig. 3, where the control volume faces are shown by continuous lines and the pressure and temperature nodes, by

dots. The extra layer of pseudo-cells used for setting the boundary conditions is also shown.

5. Results and discussion

Results are obtained for various values of Reynolds and Grashof numbers with the values of the geometrical parameters chosen as $Pr = 0.7$, $L_1^* = 0.1$, $L_2^* = 0.15$, $L_3^* = 0.25$, $L_4^* = 0.1$ and $H_1^* = 0.25$. The thermal conductivity ratio λ_s^* is varied from 1 to 100.

5.1. Pressure drop across the enclosure in pure forced convection

For low values of Re ($0 \leqslant Re \leqslant 20$), $\Delta p^*/10^6$ correlates as $0.37 \times 10^{-4} Re$ while for the range $500 \leqslant Re \leqslant 3000$, $\Delta p^*/10^6$ correlates as $3.517 \times 10^{-7} Re^{2.05}$. Following Churchill [34], the pressure drop for the range $0 \leqslant Re \leqslant 3000$ is correlated as:

$$\Delta p^*/10^6 = \left[\left(0.37 \times 10^{-4} Re\right)^2 + \left(3.517 \times 10^{-7} Re^{2.05}\right)^2\right]^{1/2} \quad (15)$$

with a standard error of estimate of 0.026 and a correlation coefficient of 0.999. The standard error of estimate is defined as [sum of the squares of error$/(l - m - 1)]^{1/2}$, where l is the number of data points, m is the number of independent variables and $l - m - 1$ is the number of degrees of freedom. In the above correlation m is taken as 2 because two correlations spanning different ranges of the independent variable are combined. The correlation coefficient is defined as $[1 -$ (sum of squares of residuals/total sum of squares)$]^{1/2}$.

5.2. Induced velocity in pure natural convection

The values of the induced velocity $v^*_{\text{in,pnc}}$ in pure natural convection ($Re = 0$, $\Delta p^* = 0$) for various values of Gr and λ_s^* are shown in Table 3. As can be seen, there is not much difference in $v^*_{\text{in,pnc}}$ with increase in λ_s^* in the Grashof number range chosen. It appears that, for a given Grashof number, the quantity $v^*_{\text{in,pnc}}$ depends only upon the heat transferred to the fluid, which, in the steady state is the same for different values of λ_s^*.

5.3. Natural convection induced velocity in the presence of mixed convection

The natural convection induced velocity $v^*_{\text{in,nc}}$ in mixed convection is plotted against the Reynolds number ($= v_{\text{in,fc}} H/\nu$) in Fig. 4 for various values of Grashof number, for a thermal conductivity ratio of 10. The values of $v^*_{\text{in,nc}}$ for $Re = 0$, of course, correspond to the pure natural convection case. It can be seen that, at a given Grashof number, the quantity $v^*_{\text{in,nc}}$ first increases until the Reynolds number reaches a moderate value, attains a peak and then begins to decrease with increasing Reynolds number. At low to moderate Reynolds numbers the natural convection tends to compete with forced convection, the former tending to produce a plume above the block surface and the latter tending to drive the flow straight upwards from the inlet. It is conjectured that during this interaction, higher temperatures occur over most of the fluid region increasing the buoyancy and hence the natural convection component of the velocity at the inlet. As shown later in the block surface temperature plots (Fig. 7), this phenomenon is attended by a slight overheating of the block surface at higher Grashof numbers (10^6 and 5×10^6). At Grashof numbers of less than or equal to 5×10^5, the overheating of the block surface is not observed. As the Reynolds number attains higher values, the natural convection component of the inlet velocity decreases and tends to become insensitive to Grashof number.

Table 3
Dimensionless induced velocity $v^*_{\text{in,pnc}}$ in pure natural convection

Gr	Solid-to-fluid thermal conductivity ratio λ_s^*			
	1	10	50	100
10^4	9.299	9.149	9.0627	8.690
5×10^4	25.424	25.470	25.690	25.000
10^5	36.720	36.880	37.150	36.470
5×10^5	79.980	80.400	80.420	79.300
10^6	109.760	110.260	109.962	108.460
5×10^6	215.140	210.320	215.958	213.630

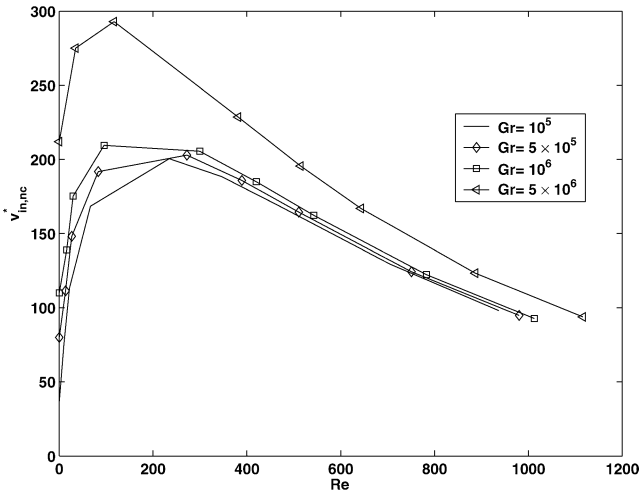

Fig. 4. Dimensionless natural convection induced velocity at the inlet in mixed convection for various Reynolds numbers for $\lambda_s^* = 10$.

5.4. Streamline and isotherm maps

The flow and temperature distributions are depicted by means of selected streamline and isotherm maps presented in Fig. 5 ($Gr = 10^5$, $\lambda_s^* = 10$) and Fig. 6 ($Gr = 10^6$, $\lambda_s^* = 10$). The stream function is defined by the line integral:

$$\psi^* = \psi^*_{\text{ref}} + \int (u^* \, \mathrm{d}y^* - v^* \, \mathrm{d}x^*) \quad (16)$$

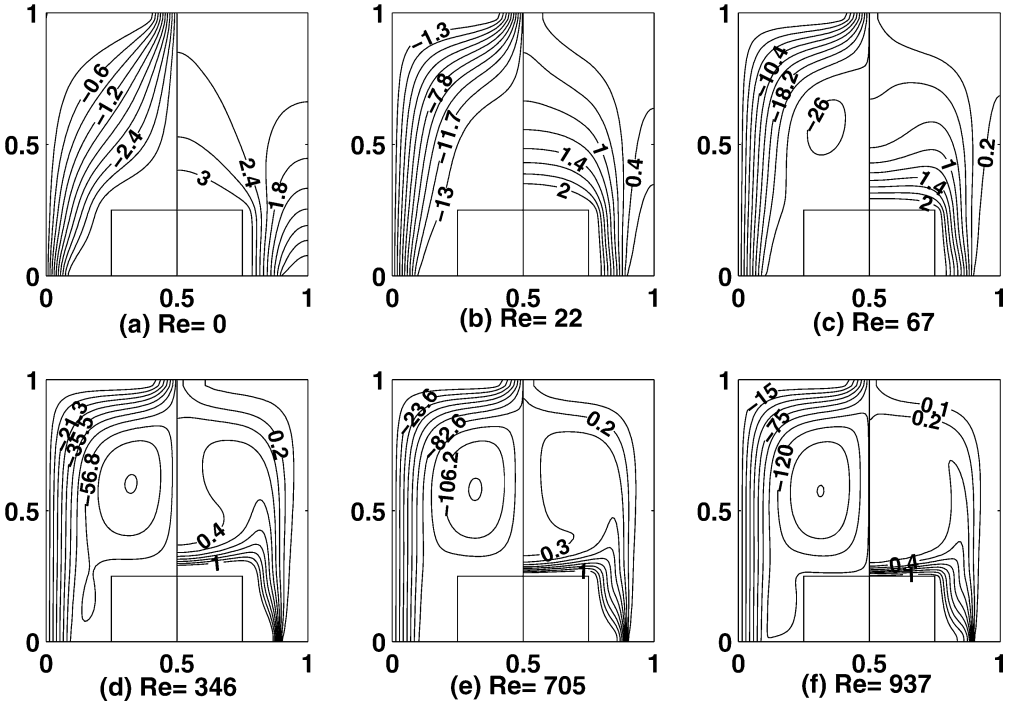

Fig. 5. Streamlines (leftside) and isotherms (rightside) for $Gr = 10^5$ and $\lambda_s^* = 10$.

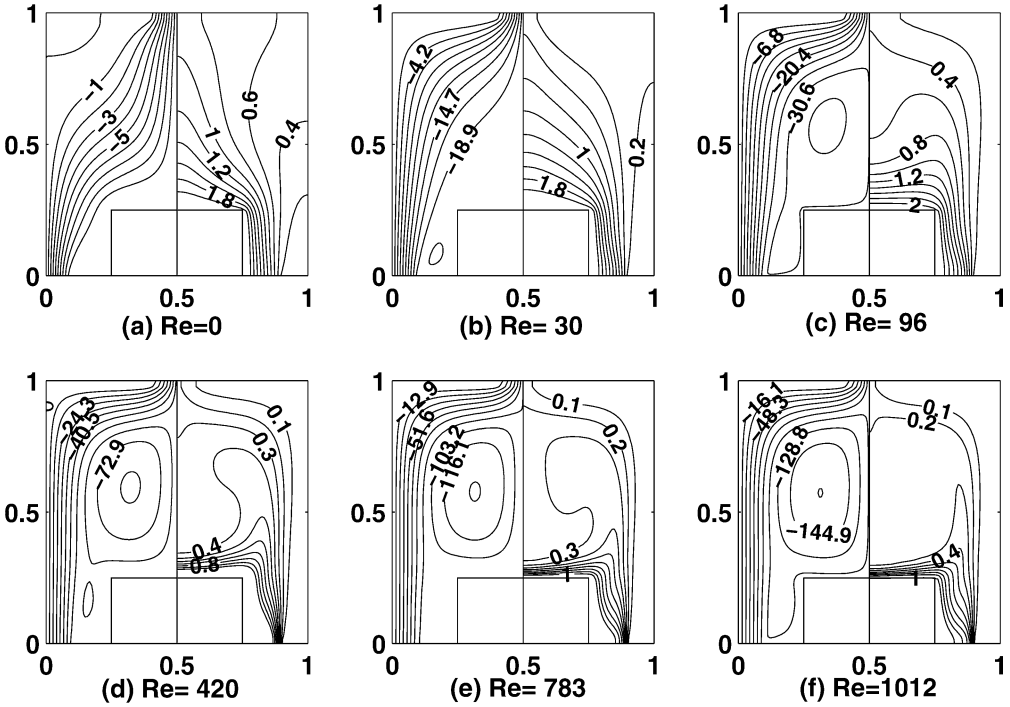

Fig. 6. Streamlines (leftside) and isotherms (rightside) for $Gr = 10^6$ and $\lambda_s^* = 10$.

where ψ_{ref}^* is the reference stream function value. In the isotherm maps, the dimensionless temperature is multiplied by a factor of 100 due to the small magnitude of T^*. The streamline and isotherm maps for each Grashof number show the general features of the flow and temperature fields. For each mixed convection run, the total dimensionless inlet velocity v_{in}^* and the Grashof number Gr are prescribed and the pressure drop across the enclosure Δp^* is determined. The value of Re for each run is obtained from Eq. (15) relating the pressure drop and the Reynolds number. The quantity v_{in}^* can then be decomposed into Re and $v_{\text{in,nc}}^*$. Considering, for instance, Fig. 5, the streamline patterns show that the

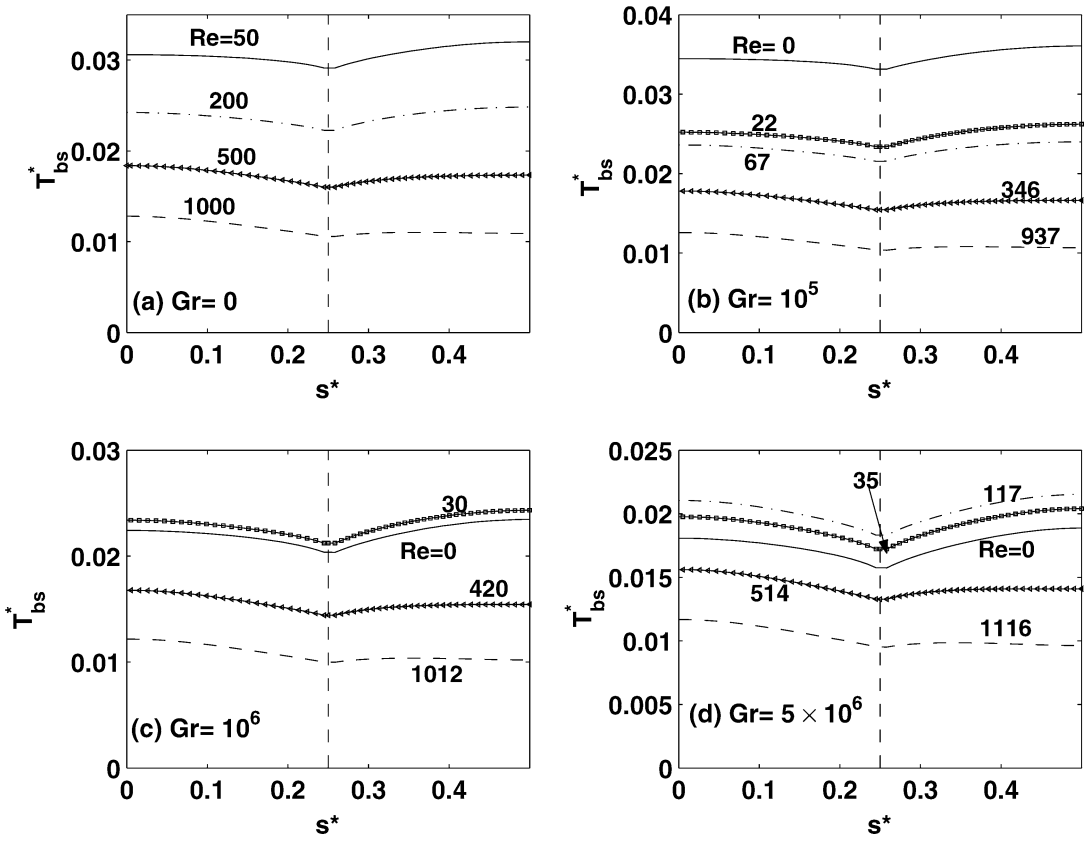

Fig. 7. Dimensionless block surface temperature variation for $\lambda_s^* = 10$.

fluid passes smoothly from entry to exit at low Reynolds numbers. As the Reynolds number increases, the fluid is increasingly directed upwards during a major part of its traverse and there occurs a recirculation region or eddy of increasing strength in the core region. The isotherms in the block are characteristic of the heat generation taking place in the block, namely, temperature decreasing from the middle portion towards the surfaces of the block. At higher *Re*, the clustering of the isotherms above the horizontal surface of the block shows that the temperature gradient is higher in this region. Fig. 6 shows a similar trend with increasing *Re*. It can also be concluded by a comparison of Figs. 5 and 6 that an increase in Grashof number at the same Reynolds number has the effect of increasing the stream function magnitudes and hence the total inlet velocity. An increase in *Gr* should also produce a stronger plume above the horizontal surface of the block tending to drive the fluid upwards into the outlet and decrease the size of the recirculation zone, although this effect is not so clearly revealed by a comparison of Figs. 5 and 6. Isotherm plots also have shown that higher thermal conductivity ratios tend to even out the temperature in the block.

5.5. Dimensionless local block surface temperature

The variation of the dimensionless block surface temperature T_{bs}^* with distance s^* (measured along the block surface CDE starting from the point C in Fig. 1(c)) for block-to-air thermal conductivity ratio of 10 is depicted in Fig. 7. The subfigures in each of these figures correspond to various Grashof numbers as shown. The values of *Re* in each subfigure are obtained from the pressure drop correlation given by Eq. (15). The segment $s^* = 0 - 0.25$ corresponds to the vertical surface of the block and the segment $s^* = 0.25 - 0.5$ corresponds to the semi-horizontal surface of the block. As s^* increases from zero to 0.25 (vertical surface), T_{bs}^* decreases and from $s^* = 0.25$ to 0.5 (horizontal surface), T_{bs}^* increases. For higher Grashof numbers, with increase in Reynolds number the block surface is slightly overheated initially and later the block surface temperature decreases with the increase in *Re*. The initial overheating is due to the complex flow field created by the interaction of the competing forced and natural convection effects at lower values of *Re*, as mentioned earlier. Although the *Re* values differ in each subfigure, it can nevertheless be concluded that at a given location on the block surface, for a given *Re*, the quantity T_{bs}^* shows decreasing trend as *Gr* is increased. Since for given fluid properties and geometric parameters, the characteristic temperature difference ΔT (based on heat generation rate) increases as *Gr* increases, the above trend means that $(T_{\mathrm{bs}} - T_{\mathrm{in}})$ increases at a slightly slower rate than ΔT. The dimensional temperature T_{bs} at any s^* and *Re*, of course, increases with *Gr*. Similar variations are observed at other values of λ_s^*. At a thermal conductivity ratio

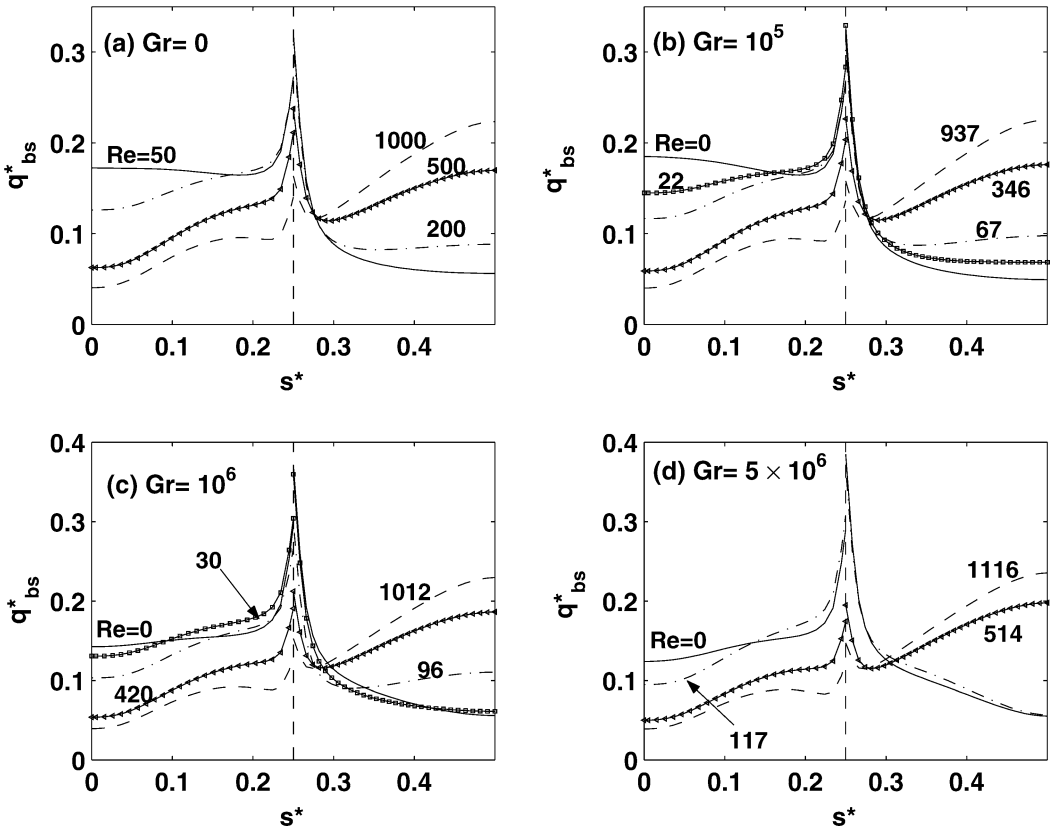

Fig. 8. Variation of the dimensionless local heat flux from the block surface for $\lambda_s^* = 10$.

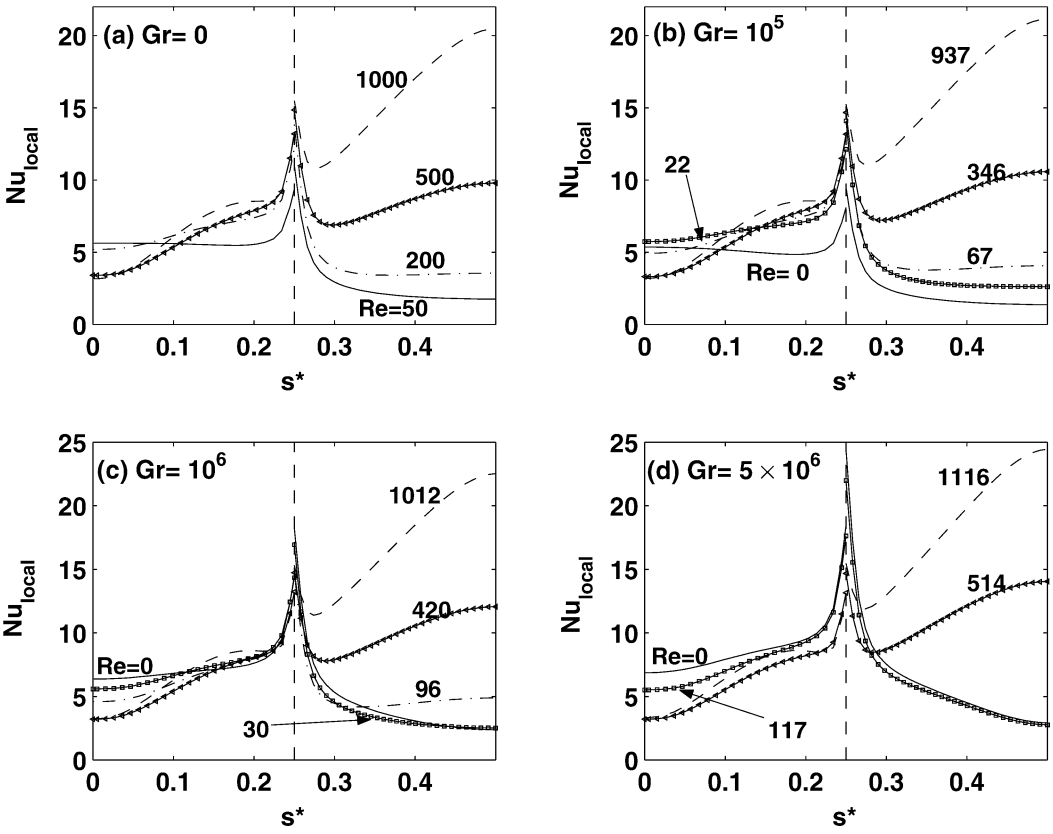

Fig. 9. Local Nusselt number variation along the block surface for $\lambda_s^* = 10$.

of 100, the drop and rise in T^*_{bs} on the vertical and horizontal block surfaces are less pronounced and the dimensionless surface temperature in general is lower compared to the case $\lambda^*_s = 10$.

5.6. Dimensionless local heat flux from the block surface

The dimensionless heat flux $\dot{q}^*_{bs}$ from the block surface is plotted against the peripheral distance s^* in Fig. 8 for $\lambda^*_s = 10$. At any *Gr*, there is a considerable variation of $\dot{q}^*_{bs}$ with s^* even for high values of *Re*. At any *Gr*, as *Re* increases, the dimensionless local heat flux on the horizontal block surface shows broadly an increasing trend. On the other hand, $\dot{q}^*_{bs}$ on the vertical surface shows more or less the opposite trend. Recalling the flow patterns from the streamline maps, it can be concluded that the heat removal from the horizontal surface of the block becomes progressively more effective as *Re* increases, due to the increasing strength of the recirculation zone above the horizontal surface. With increasing *Re*, since the eddy extends to the adjacent region of the vertical surface, here too the heat transfer coefficient can be expected to become better. However, for a particular heat generation rate, more outgoing flux from the horizontal surface means less heat removal from the vertical surface. This can be the reason for the decreasing trend of the local heat flux on the vertical surface. At a given *Re*, the variation of the dimensionless heat flux $\dot{q}^*_{bs}$ with increasing *Gr* depends upon the relative magnitudes of the dimensional flux and the heat generation based ΔT, both of which increase with *Gr*. For this reason, substantial differences do not occur in $\dot{q}^*_{bs}$ with increasing *Gr* at any s^* and *Re*.

5.7. Local Nusselt number on the block surface

The variation of the local Nusselt number is shown in Fig. 9 for a thermal conductivity ratio of 10. Since Nu_{local} can be expressed as the ratio $\dot{q}_{bs}/(T_{bs} - T_{in})$ or $\dot{q}^*_{bs}/T^*_{bs}$, its variation depends upon the relative magnitudes of the numerator and the denominator. At a given *Gr*, the local Nusselt number on the horizontal surface generally increases with increase in *Re*, although a slight initial decrease with *Re* is observed at higher *Gr*. This behaviour can be readily explained because from the earlier figures it can be observed that $\dot{q}^*_{bs}$ increases and T^*_{bs} decreases on the horizontal surface of the block at higher *Re* and a slight overheating may occur at lower *Re*. However, since both $\dot{q}^*_{bs}$ and T^*_{bs} decrease with increasing *Re* on the vertical surface, the variation of Nu_{local} can be rather complex. However, generally speaking, Nu_{local} on the vertical surface increases with increasing *Re* as shown in Fig. 9, as the local dimensionless heat flux decreases at a slower rate than the rate at which T^*_{bs} decreases with *Re*. Although the same set of *Re* values could not be chosen for different values of *Gr*, it can be seen without much difficulty that Nu_{local} increases with *Gr* at a given *Re*.

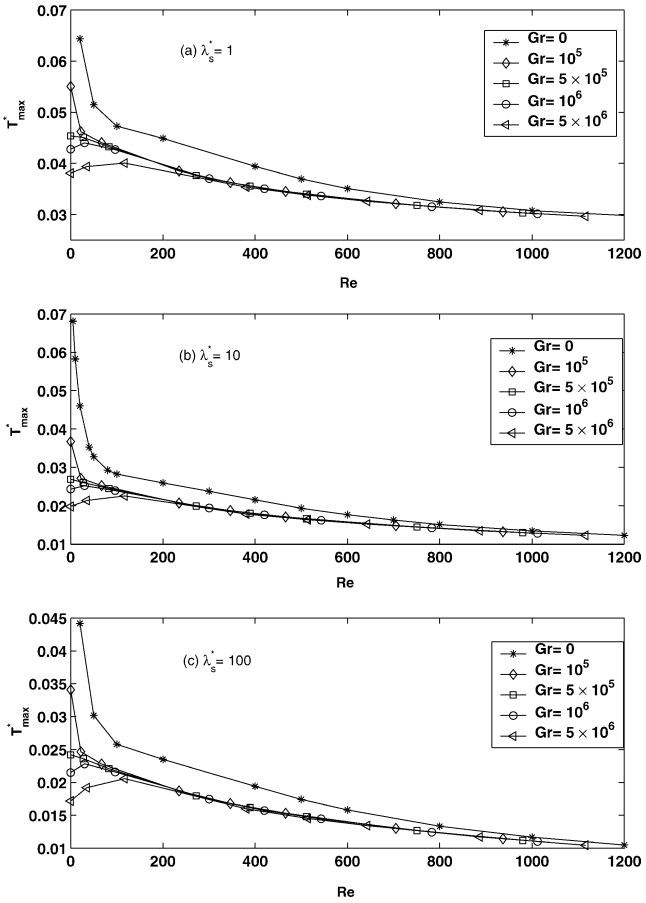

Fig. 10. Variation of the dimensionless maximum temperature with Reynolds number for various Grashof numbers (a) $\lambda^*_s = 1$, (b) $\lambda^*_s = 10$, (c) $\lambda^*_s = 100$.

5.8. Variation of maximum dimensionless temperature and Nusselt numbers

The variation of $T^*_{max}(= (T_{max} - T_{in})/\Delta T)$ with *Re* for various values of *Gr* is depicted in Fig. 10, with the subfigures applicable to various thermal conductivity ratios. While for lower values of Grashof number the quantity T^*_{max} decreases with increasing Reynolds number, for higher values of Grashof number, the same shows a slight increase first and then decreases with the increasing *Re*. Also at a given Reynolds number, T^*_{max} decreases with increasing *Gr*. Since $T_{max} - T_{in}$ and ΔT increase with *Gr*, this means that $(T_{max} - T_{in})$ increases at a smaller rate than ΔT as *Gr* increases at a particular *Re*. It can also be seen that T^*_{max} becomes insensitive to the Grashof number as Reynolds number increases. For the geometrical parameters chosen, the mixed convection regime appears to extend up to typically $Re = 600$ beyond which the mixed convection T^*_{max} values differ from corresponding forced convection values by less than 5 per cent.

As shown in Figs. 11 and 12, both Nu_1 and Nu_2 generally increase with *Re* at a given *Gr* although slight decrease in these quantities may occur at lower Reynolds numbers for

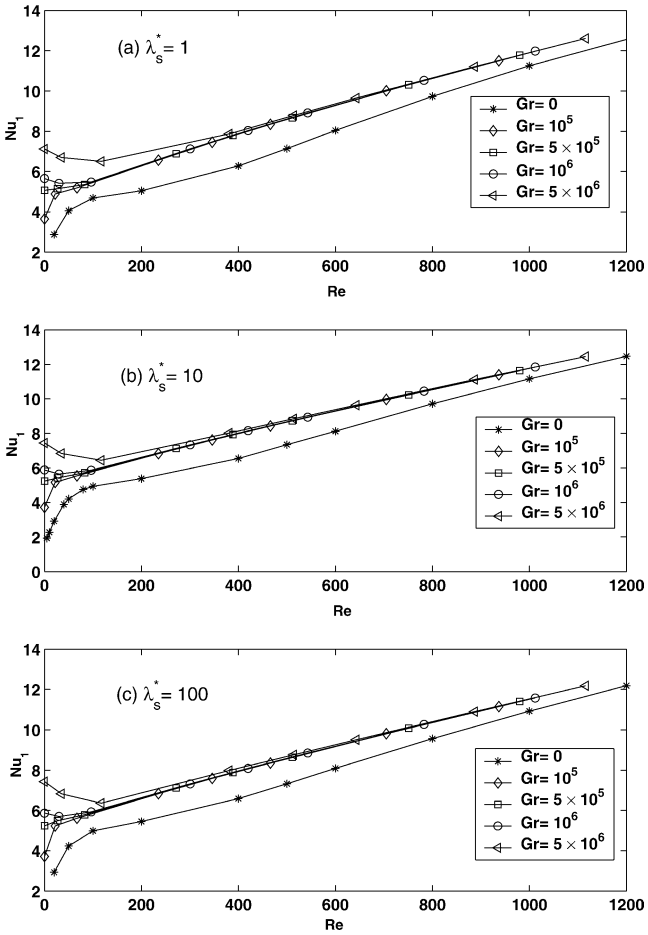

Fig. 11. Variation of the block surface average Nusselt number with Reynolds number for various Grashof numbers (a) $\lambda_s^* = 1$, (b) $\lambda_s^* = 10$, (c) $\lambda_s^* = 100$.

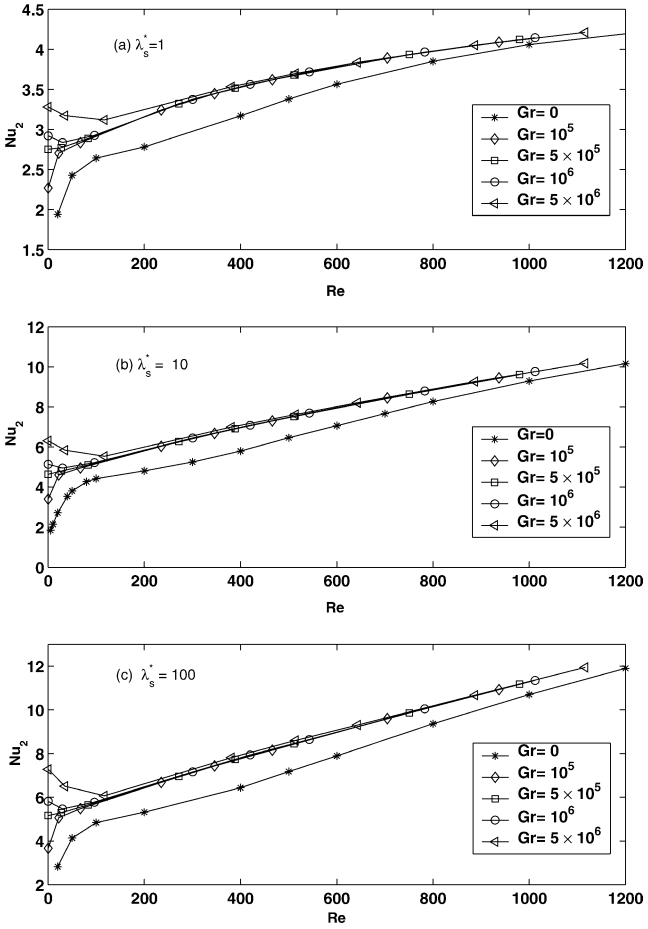

Fig. 12. Variation of the maximum temperature based Nusselt number with Reynolds number for various Grashof numbers (a) $\lambda_s^* = 1$, (b) $\lambda_s^* = 10$, (c) $\lambda_s^* = 100$.

higher values of Gr. Since Nu_2 is a measure of the reciprocal of $T^*_{\max}$, its variation with Re is opposite to that of $T^*_{\max}$.

6. Correlations from computed data

The computed data is subjected to a regression analysis using MATLAB 6.0 software in order to obtain correlations for various quantities. The correlations are shown in Table 4 along with the values of the standard error of estimate and the correlation coefficient. Following the method of constructing correlations for external flow mixed convection [4], an attempt is made to correlate $T^*_{\max}$ as:

$$\left[\frac{T^*_{\max}}{a\,Re^b}\right]^{-n} = 1 + \left\{\frac{c}{a}\left(Ar\,Re^{2-b/d}\right)^d\right\}^{-n} \tag{17}$$

where $T^*_{\max} = a\,Re^b$ and $T^*_{\max} = c\,Gr^d$ are the separate correlations for forced convection and natural convection, respectively, and n, a positive integer. However, this functional relationship is not found to be successful in correlating the data. Reexamination of the data revealed that the dimensionless maximum temperature correlates with the total dimensionless inlet velocity, as shown in Table 4, where correlations are also presented for the dimensionless natural convection velocity $v^*_{\text{in,nc}}$ in mixed convection for thermal conductivity ratios 1, 10 and 100. Although separate correlations are presented for forced convection, the correlations for $T^*_{\max}$ in mixed convection can predict the forced convection limit very well. The mixed convection correlation predicts $T^*_{\max}$ in pure natural convection with a maximum difference (at $Gr = 10^6$) of 9.9 per cent for $\lambda_s^* = 1$, 17 per cent for $\lambda_s^* = 10$ and 21 per cent for $\lambda_s^* = 100$. In view of the larger differences that may occur while using the mixed convection heat transfer correlations for pure natural convection at higher thermal conductivity ratios, it is better to use the separate correlations shown in Table 4 for predicting $T^*_{\max}$ in pure natural convection. Similarly, separate correlations given in Table 4 may be employed to predict $v^*_{\text{in,nc}}$ and $v^*_{\text{in,pnc}}$. The values of the correlation coefficient show generally a good agreement between the computed and the correlated data. The accuracy of the mixed convection correlations presented here is better in the range $100 \leqslant Re \leqslant 1129$ than in the range $0 < Re < 100$.

Table 4
Correlations obtained from regression analysis

	Régime	Variable	Correlation	S.E.E.	C.C.	Range
$\lambda_s^* = 1$	F.C.	T_{max}^*	$0.1083\,Re^{-0.177}$	0.047	0.970	$5 \leqslant Re \leqslant 1500$
	P.N.C.	T_{max}^*	$0.2271\,Gr^{-0.12}$	0.057	0.990	$10^4 \leqslant Gr \leqslant 5\times10^6$
		$v_{in,pnc}^*$	$0.1053\,Gr^{0.5}$	0.33	0.997	$10^4 \leqslant Gr \leqslant 5\times10^6$
	M.C.	$v_{in,nc}^*$	$[(17.55\,Gr^{0.051}\,Re^{0.48})^4 + (Re-40)^4]^{0.25} - Re$	0.216	0.996	$0 < Re \leqslant 1129$, $10^4 \leqslant Gr \leqslant 5\times10^6$
	Any régime	T_{max}^*	$0.108(Re+v_{in,nc}^*)^{-0.178}$	0.047	0.98	$5 \leqslant v_{in}^* \leqslant 1500$, $10^4 \leqslant Gr \leqslant 5\times10^6$
$\lambda_s^* = 10$	F.C.	T_{max}^*	$0.114\,Re^{-0.298}$	0.091	0.990	$5 \leqslant Re \leqslant 1500$
	P.N.C.	T_{max}^*	$0.317\,Gr^{-0.184}$	0.067	0.990	$10^4 \leqslant Gr \leqslant 5\times10^6$
		$v_{in,pnc}^*$	$0.1053\,Gr^{0.5}$	0.33	0.996	$10^4 \leqslant Gr \leqslant 5\times10^6$
	M.C.	$v_{in,nc}^*$	$[(17.55\,Gr^{0.051}\,Re^{0.48})^4 + (Re-40)^4]^{0.25} - Re$	0.216	0.996	$0 < Re \leqslant 1129$, $10^4 \leqslant Gr \leqslant 5\times10^6$
	Any régime	T_{max}^*	$0.114(Re+v_{in,nc}^*)^{-0.298}$	0.091	0.980	$5 \leqslant v_{in}^* \leqslant 1500$, $10^4 \leqslant Gr \leqslant 5\times10^6$
$\lambda_s^* = 100$	F.C.	T_{max}^*	$0.126\,Re^{-0.353}$	0.14	0.975	$5 \leqslant Re \leqslant 1500$
	P.N.C.	T_{max}^*	$0.33\,Gr^{-0.19}$	0.11	0.990	$10^4 \leqslant Gr \leqslant 5\times10^6$
		$v_{in,pnc}^*$	$0.1053\,Gr^{0.5}$	0.33	0.997	$10^4 \leqslant Gr \leqslant 5\times10^6$
	M.C.	$v_{in,nc}^*$	$[(17.55\,Gr^{0.051}\,Re^{0.48})^4 + (Re-40)^4]^{0.25} - Re$	0.216	0.996	$0 < Re \leqslant 1129$, $10^4 \leqslant Gr \leqslant 5\times10^6$
	Any régime	T_{max}^*	$0.136(Re+v_{in,nc}^*)^{-0.353}$	0.14	0.975	$5 \leqslant v_{in}^* \leqslant 1500$, $10^4 \leqslant Gr \leqslant 5\times10^6$

S.E.E. = Standard error of estimate; C.C. = Correlation coefficient; $v_{in}^* = Re + v_{in,nc}^*$; F.C. = Forced convection; P.N.C = Pure natural convection; M.C. = Mixed convection

7. Conclusions

A computational study of laminar mixed convection in a shallow enclosure with block-like heat generating components and inlet and outlet openings is performed neglecting the end effects and taking into account the periodic repetitions and symmetry in the geometry. A more convenient approach is adopted by decoupling the forced and free velocity components at the inlet and basing the Reynolds number on the forced component produced by fan. This gives the Reynolds number strictly its forced convection attribute unlike many earlier studies in which the Reynolds number is based on the total inlet velocity comprising both the forced and free convection components.

The results show that the velocity induced by free convection at any Grashof number first increases until the Reynolds number reaches a moderate value, attains a peak and then begins to decrease with increasing Reynolds number. The inlet velocity varies as $\sqrt{Gr}$ in pure natural convection. The block surface temperature at a given Grashof number is found to decrease with the Reynolds number monotonically for Grashof numbers less than or equal to 5×10^5. However, for higher Grashof numbers, an initial overheating followed by a decrease in block surface temperature with increasing Reynolds number is observed. As regards heat removal, the vertical and horizontal surfaces of the block show opposite trends, namely, an increase in the surface heat flux of horizontal surface resulting in a decrease in heat flux from the vertical surface and vice versa. The variation of dimensionless maximum temperature and Nusselt numbers reveal that, above a Reynolds number of typically 600, the free convection effects do not significantly influence the forced convection. The thermal conductivity ratio has a negligible effect on the velocity fields.

Acknowledgement

The authors wish to thank Dr. E. Papanicolaou, Solar and other energy systems laboratory, Demokritos, National Center for Scientific Research, Aghia Paraskevi, Attiki 15310, Greece, for providing the details of Zhu's HLPA scheme and for suggesting some papers on higher order convective schemes.

References

[1] E.G. van der Hegge Zijnen, Modified correlation formulae for the heat transfer by natural and by forced convection from horizontal cylinders, Appl. Sci. Res. A 6 (1957) 129–140.
[2] A. Acrivos, Combined laminar free and forced convection heat transfer in external flows, AIChE J. 4 (1958) 285–289.
[3] T.S. Chen, B.F. Armaly, Mixed convection in external flow, in: S. Kakaç, R.K. Shah, W. Aung (Eds.), Handbook of Single Phase Convective Heat Transfer, Wiley, New York, 1987, Section 14.
[4] S.W. Churchill, Combined free and forced convection around immersed bodies, in: E.U. Schlünder (Ed.), HEDH: Heat Exchanger Design Handbook, vol. 2: Fluid Mechanics and Heat Transfer, VDI-

Verlag/Hemisphere, Dusseldorf/Washington, DC, 1983, pp. 2.5.9-1–2.5.9-7, Section 2.5.9.
[5] W. Aung, Mixed convection in internal flow, in: S. Kakaç, R.K. Shah, W. Aung (Eds.), Handbook of Single Phase Convective Heat Transfer, Wiley, New York, 1987, pp. 15-1–15-55, Section 15.
[6] A. Bejan, Convective Heat Transfer, second ed., Wiley, New York, 1995.
[7] B. Metais, E.R.G. Eckert, Forced, mixed and free convection regimes, Trans. ASME J. Heat Transfer 86 (1964) 295–296.
[8] A.M. Dalbert, Natural, mixed and forced convection in a vertical channel with asymmetric uniform heating, in: U. Grigull, E. Hahne, K. Stephan, J. Straub (Eds.), Heat Transfer 1982: Proc. Seventh Int. Heat Transfer Conf., vol. 3, Hemisphere, Washington, DC, 1982, pp. 431–434.
[9] A.M.C. Chan, P.S. Smereka, D. Guisti, A numerical study of transient mixed convection flows in a thermal storage tank, Trans. ASME J. Solar Energy Engrg. 105 (1983) 246–253.
[10] W.L. Oberkampf, L.I. Crow, Numerical study of velocity and temperature fields in a flow-through reservior, Trans. ASME J. Heat Transfer 98 (1976) 353–359.
[11] P.V. Nielsen, A. Restivo, J.H. Whitelaw, Buoyancy affected flows in ventilated rooms, Numer. Heat Transfer 2 (1979) 115–127.
[12] P.H. Oosthuizen, J.T. Paul, Mixed convection heat transfer in a cavity, in: F.A. Kulacki, R.D. Boyd (Eds.), Fundamentals of Forced and Mixed Convection, in: ASME HTD, vol. 42, 1985, pp. 159–169.
[13] J.P. Simoneau, C. Inard, F. Allard, Numerical approach of interaction between injection and laminar natural convection in a thermally driven cavity, in: R.S. Figliola, P.G. Simpkins (Eds.), Natural Convection in Enclosures, in: ASME HTD, vol. 99, 1988, pp. 45–51.
[14] E. Papanicolaou, Y. Jaluria, Mixed convection from an isolated heat source in a rectangular enclosure, Numer. Heat Transfer A 18 (1990) 427–461.
[15] E. Papanicolaou, Y. Jaluria, Mixed convection from a localized heat source in a cavity with conducting wall: A numerical study, Numer. Heat Transfer A 23 (1993) 463–484.
[16] E. Papanicolaou, Y. Jaluria, Mixed convection from simulated electronic components at varying relative positions in a cavity, Trans. ASME J. Heat Transfer 117 (1994) 960–970.
[17] E. Papanicolaou, Y. Jaluria, Transition to a periodic regime in mixed convection in a square cavity, J. Fluid Mech. 239 (1992) 489–509.
[18] E. Papanicolaou, Y. Jaluria, Computations of turbulent flow in mixed convection with a localized heat source, Trans. ASME J. Heat Transfer 116 (1995) 649–658.
[19] C.W. How, T.H. Hsu, Transient mixed convection in a partially divided enclosure, Comput. Math. Appl. 36 (1998) 95–115.
[20] T.H. Hsu, S.G. Wang, Mixed convection in a rectangular enclosure with discrete heat sources, Numer. Heat Transfer A 38 (2000) 627–652.
[21] C.Y. Choi, A. Ortega, Mixed convection in an inclined channel with discrete heat sources, Internat. J. Heat Mass Transfer 36 (1993) 3119–3134.
[22] K.J. Kennedy, A. Zebib, Combined free and forced convection between horizontal parallel planes: some case studies, Internat. J. Heat Mass Transfer 26 (1983) 471–474.
[23] E.M. Sparrow, F. Samie, Interaction between a stream which passes through an enclosure and natural convection within the enclosure, Internat. J. Heat Mass Transfer 25 (1982) 1489–1502.
[24] L.C. Fang, Effect of mixed convection on transient hydrodynamic removal of a contaminant from a cavity, Internat. J. Heat Mass Transfer 46 (2003) 2039–2049.
[25] J.R. Dyer, Natural-convective flow through a vertical duct with a restricted entry, Internat. J. Heat Mass Transfer 21 (1978) 1341–1354.
[26] K.C. Karki, S.V. Patankar, Cooling of a vertical shrouded fin array by natural convection: a numerical study, Trans. ASME J. Heat Transfer 109 (1987) 671–676.
[27] A.C. Ku, M.L. Doria, J.R. Lloyd, Numerical modeling of unsteady buoyant flows generated by fire in a corridor, in: Sixteenth Symposium (International) on Combustion, The Combustion Institute, 1976, pp. 1373–1384.
[28] K.T. Yang, J.R. Lloyd, A.M. Kanury, K. Satoh, Modeling of turbulent buoyant flows in aircraft cabins, Combust. Sci. Technol. 39 (1984) 107–118.
[29] Y. Li, L. Baldacchino, Implementation of some higher order schemes on non-uniform grids, Internat. J. Numer. Methods Fluids 21 (1995) 1201–1220.
[30] J. Zhu, A low diffusive and oscillation-free convection scheme, Comm. Appl. Numer. Methods 7 (1991) 225–232.
[31] S.V. Patankar, Numerical Heat Transfer and Fluid Flow, Hemisphere/McGraw-Hill, Washington, DC/New York, 1980.
[32] A.A. Amsden, F.H. Harlow, A simplified MAC technique for incompressible fluid flow calculations, J. Comput. Phys. 6 (1970) 322–325.
[33] G. de Vahl Davis, Natural convection of air in a square cavity: a bench mark numerical solution, Internat. J. Numer. Methods Fluids 3 (1983) 249–264.
[34] S.W. Churchill, The Interpretation and Use of Rate Data: The Rate Concept, Scripta/McGraw-Hill, Washington, DC/New York, 1974.